

Direction-selective intertwined charge, orbital, and lattice orders under uniaxial strain in hole-doped manganite: $\text{La}_{0.75}\text{Ca}_{0.25}\text{MnO}_3$

Ju Hyeon Lee,¹ Beom Hyun Kim,^{2,*} and Bongjae Kim^{1,†}

¹*Department of Physics, Kyungpook National University, Daegu 45166, Republic of Korea*

²*Department of Physics & Astronomy, Seoul National University, Seoul 08826, Republic of Korea*

(Dated: May 28, 2026)

The complex interplay of charge, spin, orbital, and lattice degrees of freedom governs emergent phases in quantum materials, making strain a powerful control parameter. Recent advances in free-standing layer techniques have enabled extreme strains of nearly 8%, opening access to novel and often unexpected electronic and magnetic phases. Here, using a density functional theory approach, we investigate the effect of direction-selective uniaxial strain on the prototypical Jahn-Teller system $\text{La}_{1-x}\text{Ca}_x\text{MnO}_3$ ($x = 0.25$). We find that different strain directions stabilize qualitatively distinct structural, charge, and orbital responses, rather than merely different strengths of the same phase. In particular, extreme uniaxial strain selectively induces cooperative Jahn-Teller, breathing-like, and site-selective modulations, thereby enabling previously inaccessible intertwined orders in manganites. These results establish direction-selective uniaxial strain as a powerful and selective route for engineering emergent phases in quantum materials.

I. INTRODUCTION

Transition metal oxides (TMOs) provide a prototypical platform for emergent phenomena such as multiferroicity, superconductivity, and metal-insulator transitions (MIT), owing to the strong coupling among charge, spin, orbital, and lattice degrees of freedom [1, 2]. While this complexity makes their microscopic behavior challenging to describe, it also offers broad opportunities for material design. External perturbations such as chemical doping, epitaxial strain, and heterostructure engineering can be used to tune these coupled degrees of freedom and thereby access new electronic and magnetic phases [3–9].

LaMnO_3 (LMO) is a prototypical system of such intertwined physics. In the parent compound, the cooperative Jahn-Teller (JT) distortion, orbital order, and A -type antiferromagnetic (AFM) spin order are closely linked [1, 10–18], and an explanation based on the Kugel-Khomskii physics has provided the coherent picture of the intertwined orders [13, 19]. Upon hole doping by substitution of La^{3+} with Ca^{2+} or Sr^{2+} , additional carriers weaken the orbital order, promote metallicity, and alter the delicate balance between ferromagnetic (FM) and AFM exchange interactions [3, 20–29]. At higher doping, as in $\text{La}_{0.5}\text{Ca}_{0.5}\text{MnO}_3$, coupled charge, orbital, and spin orders so-called the CE -type phase emerge [25–29], highlighting the strong tunability of the intertwined orders in this family. This is schematically shown in Fig. 1.

Strain engineering offers another powerful route to controlling these competing phases [7, 30, 31]. Conventional substrate-based epitaxy has already revealed strain-induced MIT and magnetic phase transition in manganites [32–43]. However, the accessible strain range is often limited by substrate constraints and lattice re-

laxation. Recent advances in free-standing membrane techniques have substantially expanded this range, enabling extreme strains approaching 8% in both uniaxial and biaxial geometries [44, 45]. In $\text{La}_{0.7}\text{Ca}_{0.3}\text{MnO}_3$, such extreme strain has already been shown to induce phases beyond those accessible in conventional regimes [46].

These developments raise an important question: can uniaxial strain act not only as a stronger perturbation, but also as a qualitatively new tuning knob for intertwined orders? In an orthorhombic manganite, different strain directions need not produce the same response with different magnitudes; rather, they may selectively couple to octahedral tilting, rotation, and JT distortions in distinct ways, thereby stabilizing different charge, orbital, and magnetic states.

In this study, partly motivated by a previous investigation into extreme tensile strain [46], we investigate how extreme, direction-selective uniaxial strain reshapes the intertwined orders in hole-doped $\text{La}_{0.75}\text{Ca}_{0.25}\text{MnO}_3$ employing density functional theory (DFT) based analysis. We systematically apply uniaxial strain along the (100), (010), (110), and $(\bar{1}\bar{1}0)$ directions of orthorhombic LCMO and examine the resulting structural, orbital, charge, and magnetic responses. We show that different strain directions do not merely tune the strength of the same phase, but instead stabilize qualitatively distinct intertwined orders. In particular, strains along the (100) and (010) directions produce contrasting JT- and breathing-dominated responses because of the underlying orthorhombic anisotropy, whereas strains along the (110) and $(\bar{1}\bar{1}0)$ directions stabilize a new intertwined phase, which we denote as CF order, characterized by the coexistence of ferro-orbital order and C -type charge disproportionation with a FM ground state. Our results establish direction-selective uniaxial strain as a powerful route to accessing previously unreachable intertwined orders in correlated oxides.

* bomisu@gmail.com

† bongjae@knu.ac.kr

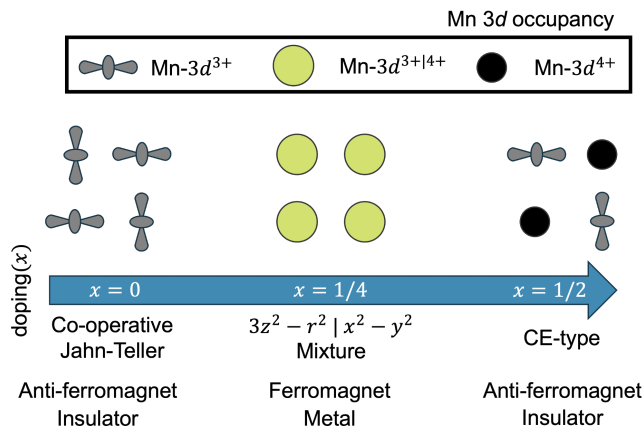


FIG. 1. Schematic phase diagram of bulk $\text{La}_{1-x}\text{Ca}_x\text{MnO}_3$ as a function of doping, x . At $x = 0$, cooperative Jahn-Teller (JT) order, accompanied by $|3x^2 - r^2\rangle/|3y^2 - r^2\rangle$ orbital ordering, is stabilized within an A -type antiferromagnetic (AFM) insulating phase. At $x = 1/4$, this orbital order is suppressed and the ferromagnetic (FM) metallic phase becomes the ground state. At half doping ($x = 1/2$), a CE -type orbital and antiferromagnetic ordered insulating phase emerges.

II. COMPUTATIONAL DETAILS

DFT calculations were performed using the Vienna *ab initio* Simulation Package (VASP) with an energy cutoff of 600 eV and an energy convergence criterion of 10^{-9} eV [47]. For the exchange-correlation functional, Perdew–Burke–Ernzerhof revised for solids (PBEsol) was employed [48]. To account for the strong octahedral rotation and tilting of the MnO_6 units (see Fig. 2(a)), we adopted an orthorhombic $Pnma$ unit cell containing 4 formula units (f.u.), corresponding to a $\sqrt{2} \times \sqrt{2} \times 2$ supercell of cubic ABO_3 . When uniaxial strain is applied, additional structural and charge orders are not captured within conventional 4 f.u. $Pnma$ cell. We therefore further expanded the cell by $\sqrt{2} \times \sqrt{2}$ in the ab plane, resulting in an 8 f.u. $2 \times 2 \times 2$ supercell. To approximate the experimentally relevant doping level of $x \approx 0.3$, we adopted a $x = 0.25$ composition, corresponding to $\text{La}_{0.75}\text{Ca}_{0.25}\text{MnO}_3$. A Monkhorst-Pack k -point mesh of $4 \times 4 \times 4$ was used.

To simulate strain, we fixed the in-plane lattice parameters (a and b) to the corresponding strained values and fully relaxed all remaining structural degrees of freedom until the residual forces were smaller than 10^{-7} eV/Å. To treat the electronic correlations in the localized Mn-3d orbitals, we employed the Hubbard correction with an on-site Coulomb interaction $U = 4$ eV and Hund’s coupling $J_H = 1$ eV [14, 49]. We note that the optimized structures show no significant dependence on the Hubbard parameters within the range considered. The chosen U value also yields structural parameters in good agreement with the fully relaxed experimental crystal structure (see

Supplementary Table S1).

III. RESULTS AND DISCUSSIONS

A. Phase diagram

In Fig. 2(b), we schematically present the full phase diagram of uniaxially strained LCMO along four representative crystallographic directions: (100), (010), (110), and $(\bar{1}\bar{1}0)$. The relation between these axes and the pseudocubic LCMO unit cell is illustrated in Fig. 2(a). Notably, the relevant phases show a clear dependence on the strain direction, which is also distinct from the biaxial-strain case.

In Figure 2(b), we schematically summarize the phase diagram of $\text{La}_{0.75}\text{Ca}_{0.25}\text{MnO}_3$ under uniaxial strain applied along four representative crystallographic directions: (100), (010), (110), and $(\bar{1}\bar{1}0)$. The relation between these directions and the axes of the pseudocubic LCMO unit cell is illustrated in Fig. 2(a). A central result is that the intertwined phases depend strongly on the direction of the applied strain, and that their evolution is qualitatively different from that found under biaxial strain (see the lower panel of Fig. 2(b)).

This directional selectivity originates from the orthorhombic $Pnma$ symmetry of LCMO, in which the MnO_6 octahedra exhibit the $a^-a^-c^+$ tilting pattern in Glazer notation. As a result, the (100) and (010) directions are not symmetrically equivalent. Under uniaxial strain along the (100) direction, the cooperative JT distortion progressively develops, whereas under strain along the (010) direction, a breathing-like modulation becomes more prominent. While the former is commonly found in manganites [36], the latter is unusual and more often associated with nickelates [50–54]. This contrast demonstrates that even within the same material, different uniaxial strain directions selectively promote distinct lattice responses, which are further reflected in the electronic structure and in the strain-driven transition from FM to an A -type AFM ground state (see Fig. 2(b)).

The response under diagonal strain, along the (110) and $(\bar{1}\bar{1}0)$ directions, is qualitatively different. Rather than being a simple combination of the (100) and (010) direction cases, they stabilize a distinct intertwined phase in which the two types of MnO_6 octahedra develop inequivalent structural and electronic characters, while the FM ground state is retained. We denote this phase as CF order, characterized by the coexistence of ferro-orbital order in the same types of MnO_6 octahedra, C -type charge disproportionation in distinct types, and a FM metallic state. While this phase is reminiscent of the coupled charge-orbital textures of conventional CE -type ordering, it differs fundamentally in its metallic ferromagnetic nature and C -type orbital order in the same types of MnO_6 octahedra. The emergence of this phase points to physics beyond Kugel-Khomskii picture [19].

We also compared our phase diagram with that ob-

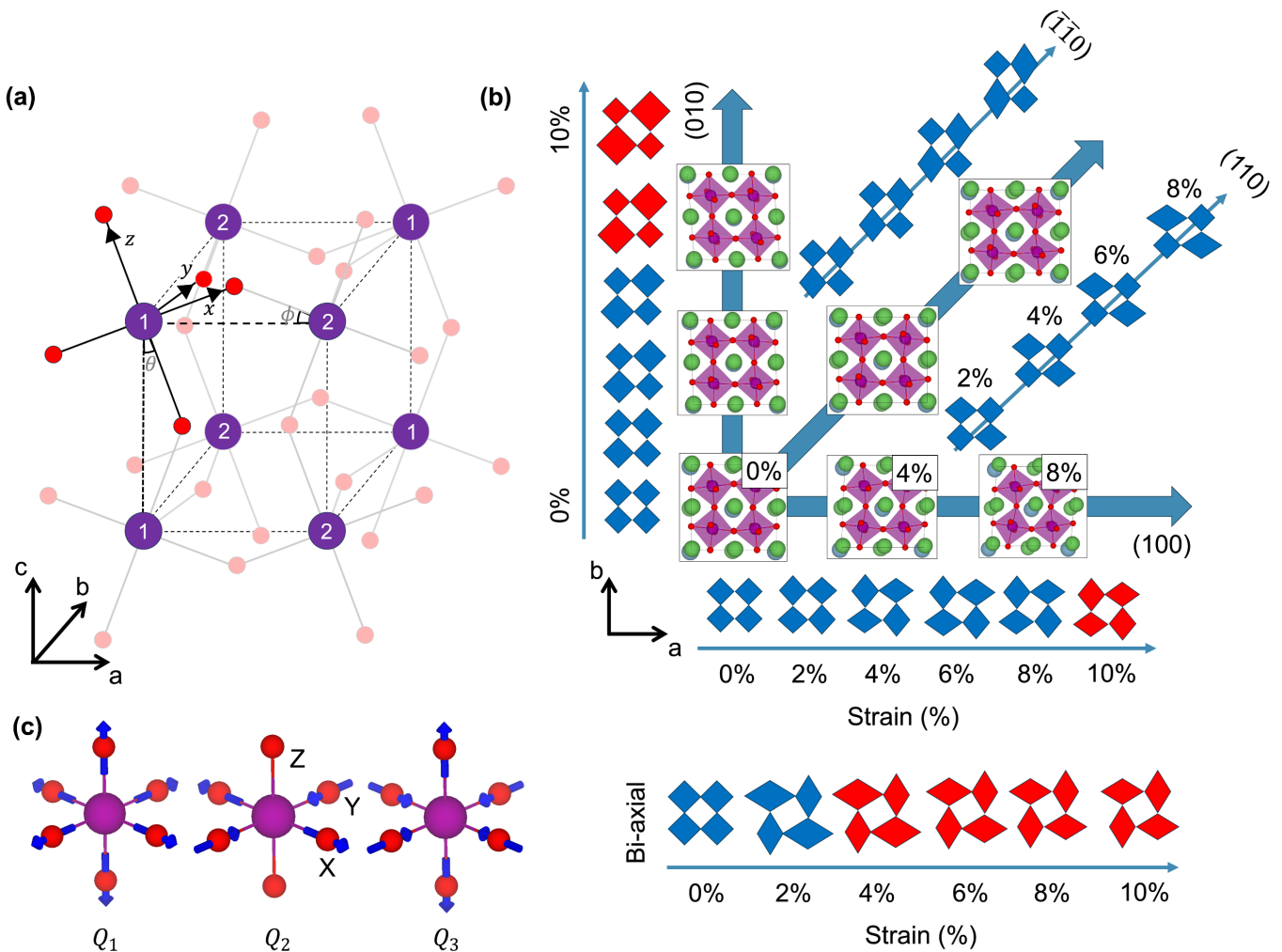


FIG. 2. (a) Schematic pseudocubic lattice of $\text{La}_{0.75}\text{Ca}_{0.25}\text{MnO}_3$ (LCMO), indicated by dashed lines. The two inequivalent Mn sites are labeled 1 and 2. ϕ and θ denote the in-plane rotation and out-of-plane tilting angles, respectively. Purple and red spheres represent Mn and O atoms. The a , b , and c axes denote the global crystallographic axes, while x , y , and z denote the local axes of the MnO_6 octahedron. (b) Schematic structural, electronic, and magnetic phase diagrams for different strain directions. Rhombus represent MnO_6 units, with their shapes and sizes indicating the type and magnitude of the distortion. Red and blue indicate ferromagnetic (FM) and A -type antiferromagnetic (AFM) ground states, respectively. (c) Schematic illustration of the symmetric breathing mode Q_1 and the asymmetric Jahn-Teller modes Q_2 and Q_3 , corresponding to orthorhombic and tetragonal distortions, respectively. Here, X , Y , and Z are the Mn-O bond lengths along the local x , y , and z axes.

tained under extreme biaxial strain. The FM-to-AFM phase transition has been proposed as the origin of the MIT in this system [46], and this behavior is reproduced in our calculations. Under biaxial strain, breathing distortion and cooperative JT modes evolve in a more intertwined manner, and the magnetic transition is triggered at lower strain than in the uniaxial cases (see Fig. 2(b)). In our calculations, the transition occurs at 4% strain, which is slightly higher than the 3% reported in previous work, likely due to small differences in the computational setup. The magnetic transition data for all studied strain directions are shown in Supplementary Fig. S1.

Overall, the stark differences in the structural, electronic, and magnetic responses among the four uniax-

ial strain directions demonstrate that extreme uniaxial strain acts as a highly selective tuning knob that goes beyond the capabilities of conventional substrate-based biaxial strain engineering. In the following sections, we show how these distinct phases arise from the underlying local structural modulations.

B. Structural response

To quantify the intertwined structural, charge, and orbital orders, we identify the relevant lattice modes of the system, as schematically shown in Fig. 2(c). The structural response of LCMO can be described in terms of

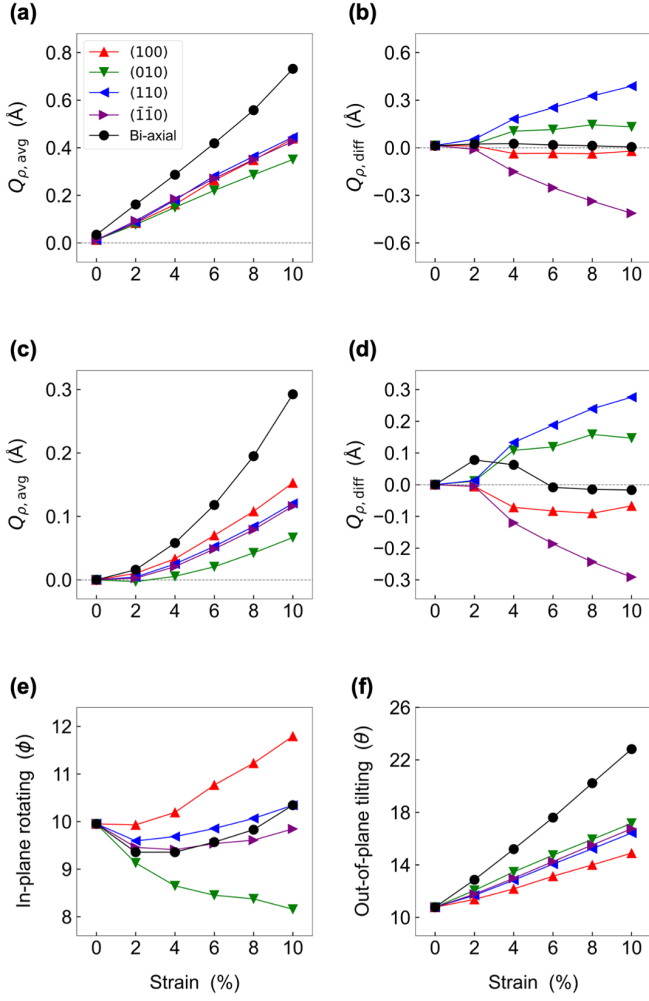


FIG. 3. Strain dependence of the averaged and site-difference of the asymmetric Jahn-Teller mode in (a) and (b), and of the breathing mode in (c) and (d), under uniaxial and biaxial strain. (e) and (f) show the in-plane rotation angle ϕ and out-of-plane tilting angle θ of the MnO_6 octahedra, respectively, as defined in Fig. 2(a).

the symmetric mode Q_1 and the asymmetric JT modes Q_2 and Q_3 , as is typical for $Pnma$ TMO perovskites. The Q_1 mode corresponds to a breathing-type distortion, whereas Q_2 and Q_3 represent orthorhombic and tetragonal distortions, respectively. The mode amplitudes are defined as $Q_{1,i} = \frac{X_i + Y_i + Z_i}{\sqrt{3}}$, $Q_{2,i} = \frac{X_i - Y_i}{\sqrt{2}}$, and $Q_{3,i} = \frac{2Z_i - X_i - Y_i}{\sqrt{6}}$, where i denotes the MnO_6 site index, and X_i , Y_i , and Z_i denote Mn–O bond-length differences along the local x , y , and z axes, respectively (see Fig. 2(a)). Unlike the conventional cooperative JT distortion, the extreme-strain regime exhibits pronounced site selectivity. In other words, a given mode develops cooperatively on both sites 1 and 2, or becomes enhanced predominantly on only one of them. To quantify this behavior, we define $Q_{1,\text{avg}} = \sum_{i=1,2} Q_{1,i}/2$ and $Q_{1,\text{diff}} = \sum_{i=1,2} (-1)^{i+1} Q_{1,i}$, where the former and the

latter represent the average amplitude and site difference of the Q_1 mode, respectively. For the asymmetric JT modes, we similarly define $Q_{\rho,\text{avg}} = \sum_{i=1,2} \rho_i/2$ and $Q_{\rho,\text{diff}} = \sum_{i=1,2} (-1)^{i+1} \rho_i$, where $\rho_i = \sqrt{Q_{2,i}^2 + Q_{3,i}^2}$ characterizes the combined amplitude of the Q_2 and Q_3 distortions at each site.

A notable common feature of LCMO under extreme strain is the emergence of the breathing mode Q_1 , regardless of the strain direction. A charge-ordered pattern of this type has not been reported in $\text{La}_{1-x}\text{Ca}_x\text{MnO}_3$ ($x \leq 0.5$) under conventional epitaxy-based effective strains, which are typically much smaller due to lattice relaxations [55, 56]. Moreover, the resulting two-dimensional checkerboard-like Q_1 modulation is fundamentally different from the breathing distortions reported in nickelates [50–52] and other TMO systems [57–59]. The appearance of Q_1 modulation in doped manganites, therefore, expands the diversity of accessible structural and electronic phases.

We first consider the biaxial-strain case. As shown in Fig. 3(a) and (b), the average JT distortion $Q_{\rho,\text{avg}}$ increases almost linearly with strain, whereas $Q_{\rho,\text{diff}}$ remains almost muted, indicating little site differentiation up to 10% strain. The behavior of the breathing distortion is markedly different. As shown in Fig. 3(c) and (d), $Q_{1,\text{avg}}$ increases sharply, especially at and above 4% strain, indicating that the Q_1 modulation emerges only beyond the conventional substrate-engineering regime. A finite $Q_{1,\text{diff}}$ appears around 2 to 4%, showing that the breathing distortion initially develops a site-selective character together with the cooperative JT response. At higher strain, however, this site selectivity is suppressed again, as evidenced by the reduction of $Q_{1,\text{diff}}$.

For the uniaxial strain, the structural response becomes strongly direction dependent. In the pseudocubic unit cell, strain applied along the (100) and (010) directions acts along diagonal directions (See Fig. 2(b)) and therefore directly modifies the in-plane rotation of the MnO_6 octahedra. Because these two directions are not symmetry-equivalent in orthorhombic LCMO, their structural responses differ substantially. As shown in Fig. 3(e), the in-plane rotation increases under strain along (100), but decreases under strain along (010), directly demonstrating the anisotropic structural response of the system.

This inequivalence is also evident in the responses of the asymmetric JT and breathing modes. Both strain directions enhance the amplitudes of these modes, as shown in Fig. 3(a) and (c), with a stronger overall modulation for strain along (100), consistent with the increase in in-plane octahedral rotation shown in Fig. 3(e). However, the site selectivity is more pronounced for strain along (010). In particular, $Q_{\rho,\text{diff}}$ becomes activated above 4% strain for the (010) case, whereas it is vanishingly small for the (100) case (Fig. 3(b)). Likewise, a nonzero $Q_{1,\text{diff}}$ appears in both cases above about 4% strain, but its magnitude is clearly larger under strain along (010). These

results indicate that strain along (100) mainly enhances cooperative JT distortion and lifts the e_g orbital degeneracy through orthorhombic distortion, whereas strain along (010) promotes a more site-selective response in which the breathing component plays a more prominent role. This distinction becomes clearer in the next subsection through the orbital-resolved analysis.

For uniaxial strain along the (110) and $(\bar{1}\bar{1}0)$ directions, the response is qualitatively different. In these cases, the strain is applied directly along the Mn–O bond directions in the pseudocubic cell, which strongly restricts the in-plane octahedral rotation as shown in Fig. 3(e). As a result, the lifting of the e_g degeneracy is governed primarily by the asymmetric responses of the JT.

The site selectivity becomes especially strong for these diagonal strain directions, as seen in Fig. 3(b). The JT distortion develops predominantly on one type of MnO_6 octahedron, while it is suppressed on the other. This asymmetry is mirrored in the breathing Q_1 mode. Indeed, Fig. 3(d) shows the opposite trends for the two sites. These results demonstrate that the direction of uniaxial strain can selectively activate or suppress specific lattice responses, thereby determining which structural modulations become dominant. Notably, the FM ground state remains stable throughout the entire strain range studied [60].

We further note that $Q_{\rho,\text{avg}}$ is significantly larger under biaxial strain than under uniaxial strain. At the same nominal in-plane strain value, biaxial strain imposes a larger two-dimensional in-plane stress, which in turn promotes stronger out-of-plane tilting, as shown in Fig. 3(a) and (f). More detailed structural information, including lattice parameters, volume changes, and bond-length evolution under strain, is provided in Supplementary Figs. S2 and S3.

An important ingredient underlying the diversity of strain-dependent behavior is hole doping. In undoped LMO, which has a similar orthorhombic structure, site-selective modulation is strongly suppressed for all uniaxial strain directions. Although the orthorhombicity-driven responses of the JT and breathing modes are qualitatively similar, the additional holes in LCMO promote instability and activate site-selective modulations, going beyond the behavior found in LMO [61, 62]. Detailed results for LMO are provided in Supplementary Fig. S4.

C. Orbital and charge order

The structural responses described above are directly reflected in the orbital and charge degrees of freedom in LCMO. The cooperative JT distortion and its site-selective character can be quantified by introducing an orbital angle at each site i , $\Phi_i = \tan^{-1}\left(\frac{Q_{2,i}}{Q_{3,i}}\right)$. This orbital angle Φ_i characterizes the orbital polarization associated with the Q_2 and Q_3 modes, which lifts the twofold

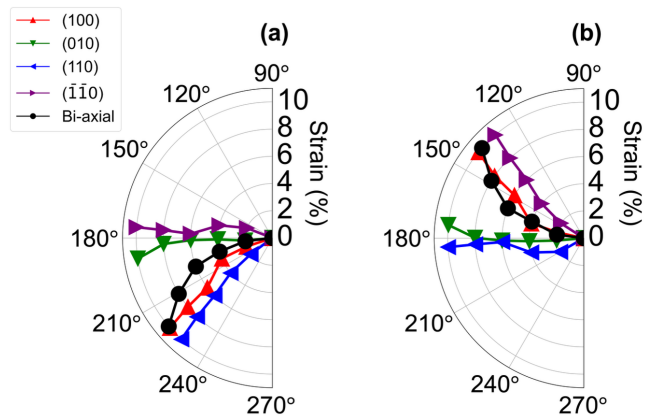


FIG. 4. Orbital angles for Mn sites 1 and 2, shown in (a) and (b), respectively, defined as $\tan^{-1}(Q_2/Q_3)$ (see Fig. 2(a) for the site labels). The orbital characters $|3x^2 - r^2\rangle$, $|3y^2 - r^2\rangle$, and $|x^2 - y^2\rangle$ correspond to orbital angles of 120° , 240° , and 180° , respectively. The black, red, green, blue, and purple curves represent biaxial strain and uniaxial strain applied along the (100), (010), (110), and $(\bar{1}\bar{1}0)$ directions, respectively.

degeneracy of the e_g orbitals and describes the relative contributions of the two JT modes [63, 64].

Figure 4 shows the evolution of the orbital angle for the two inequivalent Mn sites under various strain conditions. In unstrained LCMO, no pronounced charge or orbital order is found. In this case, the near-degeneracy between the $|x^2 - y^2\rangle$ and $|3z^2 - r^2\rangle$ states is largely preserved on both sites. Under biaxial strain, however, a cooperative distortion gradually develops, as indicated by the symmetric evolution of the two sites toward $|3y^2 - r^2\rangle$ and $|3x^2 - r^2\rangle$ character, respectively (see the black curve in Fig. 4). This corresponds to the development of a staggered orbital order.

For uniaxial strain, we again find a strong directional dependence. Under strain along (100), similarly to the biaxial case, cooperative JT distortion progressively develops in a staggered pattern. In particular, above 4% strain, a clear tendency toward the $|3y^2 - r^2\rangle/|3x^2 - r^2\rangle$ orbital order emerges. By contrast, under strain along (010), no such staggered orbital pattern develops; instead, both sites evolve toward a more pronounced $|x^2 - y^2\rangle$ character. This asymmetric response to in-plane strain originates from the orthorhombic symmetry of the system, consistent with the structural response discussed above. Strain applied along (100) is primarily accommodated within the ab plane, enhancing the in-plane octahedral rotation and thereby promoting staggered orbital order. In contrast, strain along (010) is absorbed more strongly through out-of-plane tilting, as shown in Fig. 3(f), which suppresses the tendency toward staggered in-plane orbital order. This contrast is also evident in the partial charge densities shown in Fig. 5: under strain along (100), the $|3y^2 - r^2\rangle/|3x^2 - r^2\rangle$ orbital order is clearly developed, whereas under strain along

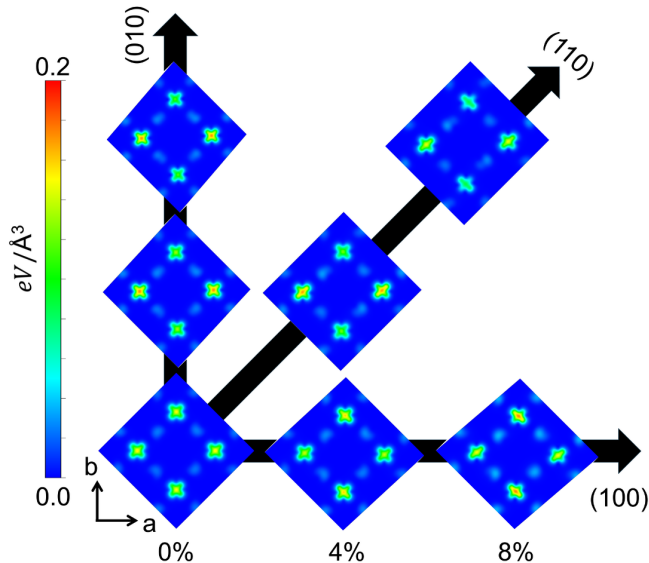


FIG. 5. Partial charge density for the occupied e_g character along the c axis (Fig. 2 (b)) is presented. The strain along (100) and (010) directions has different orbital characters, which are $|3x^2 - r^2\rangle$ or $|3y^2 - r^2\rangle$ and $|x^2 - y^2\rangle$, respectively. Further, the two different Mn sites have different electron occupancies. While the strain along (110) and $(\bar{1}\bar{1}0)$ directions has (100) and (010) directions orbital character, in between.

(010), the $|x^2 - y^2\rangle$ character is preferred.

For strain along the (110) and $(\bar{1}\bar{1}0)$ directions, yet another type of orbital order emerges. As discussed above, the two inequivalent Mn sites become strongly differentiated: one site develops orbital polarization toward $|3y^2 - r^2\rangle$ or $|3x^2 - r^2\rangle$, while the other largely retains $|x^2 - y^2\rangle$ character. This establishes new CF -type order introduced above, characterized by the coexistence of ferro-orbital order, C -type charge disproportionation, and a FM ground state. Such strong site selectivity, already evident in the breathing mode Q_1 , is also reflected in the asymmetric JT modes Q_2 and Q_3 . The partial charge density for strain along (110) clearly shows the coexistence of $|3x^2 - r^2\rangle$ -like and $|x^2 - y^2\rangle$ -like orbital characters in the MnO_6 octahedra for enhanced and suppressed Q_1 modes, respectively, providing a direct real-space signature of the CF -type order (Fig. 5). This partially polarized orbital state, originating from the asymmetric JT response together with the breathing distortion, may be viewed as intermediate between the states realized under strain along (100) and (010), and gives rise to a distinct direction-selective phase.

Beyond the orbital shapes themselves, Fig. 5 also reveals the development of charge modulation. For example, under strain along (100), the charge density differs clearly between the two Mn sites, indicating site-selective charge disproportionation. Under strain along (010), where breathing distortion and JT modulation coexist, the charge modulation becomes even stronger.

This shows that the inequivalence between the two Mn sites, already identified from the local structural analysis, is also manifested in the charge sector. The difference in the local Mn magnetic moments between the two sites further highlights the direction-dependent nature of the strain-induced charge ordering [65] (see Supplementary Fig. S5).

These unique charge-orbital-lattice patterns are not prominent at strains of 2% or less. Both orbital polarization and charge modulation become pronounced only beyond this regime. As discussed above, similar threshold behavior is also found in the structural response, where the site-selective breathing mode emerges only at strains of 4% and higher. This highlights the potential of the extreme-strain technique to access phases beyond the reach of conventional substrate engineering in complex materials.

Having established the strain-dependent orbital and charge patterns, we now turn to their connection with the magnetic phase transitions.

D. Magnetic phase transition

Undoped LMO is an A -type AFM insulator. This magnetic ground state is commonly understood in terms of Kugel-Khomskii-type superexchange coupled to cooperative Jahn-Teller distortion and the associated C -type orbital order [13, 19]. The staggered $|3x^2 - r^2\rangle/|3y^2 - r^2\rangle$ orbital pattern promotes FM exchange within the ab plane, whereas the ferro-orbital alignment along the c axis favors AFM coupling. Although the tilting and rotation of MnO_6 octahedra can delicately modulate the balance of magnetic exchange interactions between neighboring Mn sites [66, 67], the superexchange mechanism coupled with cooperative JT distortion remains the main contribution to the magnetic ground state.

Upon hole doping, the partially occupied e_g states become mobile and can hop through the lattice. This delocalization drives the double-exchange mechanism, which stabilizes the emergent FM metallic phase [61, 68]. The robustness of the FM ground state near $x \approx 0.3$ indicates that double-exchange dominates over the competing AFM superexchange in this doping regime. Under external strain, structural distortions can significantly modify this balance of magnetic exchanges, potentially driving the system away from the FM ground state. This predicted magnetic phase transition is schematically illustrated in Fig. 2(b).

Our results show that under biaxial strain, the transition from an FM to an A -type AFM state occurs at approximately 4% strain, while the metallic phase remains robust. In contrast, under uniaxial strain along the (100) and (010) directions, the magnetic transition requires significantly higher strain than in the biaxial case. Remarkably, no phase transition is observed up to 8% strain when applied along the (110) and $(\bar{1}\bar{1}0)$ directions. As shown in Fig. 3(a) and (c), the magnitudes

of both the JT distortion strength ($Q_{\rho,\text{avg}}$) and the average Mn–O bond-length ($Q_{1,\text{avg}}$) are significantly larger under biaxial strain than under uniaxial strain. These enhanced distortions suggest a suppression of e_g orbital hopping, thereby weakening the double-exchange, while simultaneously stabilization of C -type orbital ordering that favors A -type AFM superexchange.

However, the reason why the FM-to-AFM ground state transition occurs more readily under strain along (100)/(010) directions compared to strain along (110)/($\bar{1}\bar{1}0$) directions cannot be understood solely in terms of the conventional structural parameters $Q_{\rho,\text{avg}}$, $Q_{1,\text{avg}}$, ϕ , and θ (Fig. 3(a), (c), (e), and (f)), which do not show a simple trend across the magnetic phase boundary. Instead, the site-selective components $Q_{\rho,\text{diff}}$ and $Q_{1,\text{diff}}$ appear to correlate more directly with the magnetic transition. In particular, smaller site-to-site differences in these modes tend to facilitate the FM-to-AFM transition, whereas larger site selectivity stabilizes the FM phase. This suggests that the CF -type order plays an important role in the magnetic response, either by suppressing the development of A -type AFM correlations or by further stabilizing the FM metallic state, depending on the strain direction.

In the previous report by Hong *et al.*, based on an ordered-cation model, the magnetic transition was proposed as the origin of the MIT inferred from the resistivity data [46]. Due to the difference in the computational setups, such as doping level and cation order, we did not find the MIT within our studied strain ranges. Nevertheless, our results show that directional strain provides access to an even richer landscape of intertwined orbital, charge, and spin phases. Overall, the magnetic phase diagram confirms that extreme, direction-selective uniaxial strain acts as a highly selective tuning knob for intertwined orders in LCMO.

IV. CONCLUSION

In conclusion, we studied $\text{La}_{0.75}\text{Ca}_{0.25}\text{MnO}_3$ under extreme, direction-selective uniaxial strain and showed that the resulting structural, electronic, and magnetic responses depend strongly on the strain direction. Rather than producing a simple quantitative tuning of a known phase, different uniaxial strain directions stabilize qualitatively distinct intertwined orders through selective control of local octahedral distortions.

Strain along the (100) and (010) directions leads to contrasting cooperative JT and breathing-dominated responses, while strain along the (110) and ($\bar{1}\bar{1}0$) directions stabilizes a novel CF -type phase with coexisting ferro-orbital order, C -type charge disproportionation, and a FM metallic ground state. These results highlight the crucial role of site-selective lattice response in determining the emergent phases.

Overall, our work establishes extreme uniaxial strain as a highly selective tuning knob for accessing previously unreachable intertwined orders in correlated oxides, and suggests a general route for engineering emergent phases through the coupled charge, orbital, spin, and lattice degrees of freedom.

ACKNOWLEDGMENTS

We thank S. S. Hong for fruitful discussions. We also thank the participants of the conference [APCTP-2025-C01] held at PCS-IBS, Daejeon, Korea, for fruitful discussions. This work was supported by the National Research Foundation of Korea(NRF) grant funded by the Korea government(MSIT) (Grants No. RS-2024-00401881, No. RS-2026-25472078, and No. RS-2022-NR068223) and KISTI Supercomputing Center (Project No. KSC-2023-CRE-0413). The work at SNU was supported by the Leading Researcher Program of the National Research Foundation of Korea (Grant No. RS-2020-NR049405).

-
- [1] M. Imada, A. Fujimori, and Y. Tokura, Metal-insulator transitions, *Rev. Mod. Phys.* **70**, 1039 (1998).
 - [2] C. N. R. Rao, Transition metal oxides, *Annu. Rev. Phys. Chem.* **40**, 291 (1989).
 - [3] A. P. Ramirez, Colossal magnetoresistance, *J. Phys.: Condens. Matter* **9**, 8171 (1997).
 - [4] D. G. Schlom, L.-Q. Chen, C.-B. Eom, K. M. Rabe, S. K. Streiffer, and J.-M. Triscone, Strain tuning of ferroelectric thin films*, *Annu. Rev. Mater. Res.* **37**, 589 (2007).
 - [5] J. Ngai, F. Walker, and C. Ahn, Correlated oxide physics and electronics, *Annu. Rev. Mater. Res.* **44**, 1 (2014).
 - [6] A. Chen, Q. Su, H. Han, E. Enriquez, and Q. Jia, Metal Oxide Nanocomposites: A Perspective from Strain, Defect, and Interface, *Adv. Mater.* **31**, 1803241 (2019).
 - [7] T. Li, S. Deng, H. Liu, and J. Chen, Insights into Strain Engineering: From Ferroelectrics to Related Functional Materials and Beyond, *Chem. Rev.* **124**, 7045 (2024).
 - [8] J. B. Goodenough, Perspective on Engineering Transition-Metal Oxides, *Chem. Mater.* **26**, 820 (2014).
 - [9] S. Okamoto, N. Mohanta, H. N. Lee, A. Moreo, and E. Dagotto, Novel phenomena in transition-metal oxide thin films and heterostructures with strong correlations and spin-orbit coupling, *Phys. Rev. Mater.* **9**, 050301 (2025).
 - [10] J. B. Goodenough, Theory of the Role of Covalence in the Perovskite-Type Manganites $[\text{La}, M(\text{II})]\text{MnO}_3$, *Phys. Rev.* **100**, 564 (1955).
 - [11] J. He and C. Franchini, Screened hybrid functional applied to $3d^0 \rightarrow 3d^8$ transition-metal perovskites LaMO_3

- ($M = \text{Sc-Cu}$): Influence of the exchange mixing parameter on the structural, electronic, and magnetic properties, *Phys. Rev. B* **86**, 235117 (2012).
- [12] J.-H. Park, C. T. Chen, S.-W. Cheong, W. Bao, G. Meigs, V. Chakarian, and Y. U. Idzerda, Electronic Aspects of the Ferromagnetic Transition in Manganese Perovskites, *Phys. Rev. Lett.* **76**, 4215 (1996).
- [13] E. Pavarini and E. Koch, Origin of Jahn-Teller Distortion and Orbital Order in LaMnO_3 , *Phys. Rev. Lett.* **104**, 086402 (2010).
- [14] J. H. Lee and B. Kim, Revisiting LaMnO_3 : A density functional theory study, *Curr. Appl. Phys.* **78**, 7 (2025).
- [15] E. Dagotto, T. Hotta, and A. Moreo, Colossal magnetoresistant materials: the key role of phase separation, *Phys. Rep.* **344**, 1 (2001).
- [16] A. Yamasaki, M. Feldbacher, Y.-F. Yang, O. K. Andersen, and K. Held, Pressure-Induced Metal-Insulator Transition in LaMnO_3 Is Not of Mott-Hubbard Type, *Phys. Rev. Lett.* **96**, 166401 (2006).
- [17] M. Purevdorj and M.-W. Kim, Orbital wave in the Raman scattering cross section of LaMnO_3 , *Phys. Rev. B* **97**, 085101 (2018).
- [18] L. Celiberti, A. Ehrentraut, L. Leoni, and C. Franchini, Machine learning the order-disorder Jahn-Teller transition in LaMnO_3 , *The Journal of Chemical Physics* **164**, 174703 (2026).
- [19] D. I. Khomskii and S. V. Streltsov, Orbital Effects in Solids: Basics, Recent Progress, and Opportunities, *Chem. Rev.* **121**, 2992 (2021).
- [20] P. R. Sagdeo, S. Anwar, and N. P. Lalla, Powder X-ray diffraction and Rietveld analysis of $\text{La}_{1-x}\text{Ca}_x\text{MnO}_3$ ($0 < x < 1$), *Powder Diffr.* **21**, 40 (2006).
- [21] K. I. Kugel and D. I. Khomskii, The Jahn-Teller effect and magnetism: transition metal compounds, *Sov. Phys. Uspekhi* **25**, 231 (1982).
- [22] O. N. Mryasov, R. F. Sabiryanov, A. J. Freeman, and S. S. Jaswal, Effect of lattice distortions on the competition between the double and superexchange mechanisms in LaMnO_3 , *Phys. Rev. B* **56**, 7255 (1997).
- [23] T. Mizokawa, D. I. Khomskii, and G. A. Sawatzky, Interplay between orbital ordering and lattice distortions in LaMnO_3 , YVO_3 , and YTiO_3 , *Phys. Rev. B* **60**, 7309 (1999).
- [24] H. Y. Hwang, S.-W. Cheong, P. G. Radaelli, M. Marezio, and B. Batlogg, Lattice Effects on the Magnetoresistance in Doped LaMnO_3 , *Phys. Rev. Lett.* **75**, 914 (1995).
- [25] T. Hotta and E. Dagotto, Competition between ferromagnetic and charge-orbital ordered phases in $\text{Pr}_{1-x}\text{Ca}_x\text{MnO}_3$ for $x = \frac{1}{4}$, $\frac{3}{8}$, and $\frac{1}{2}$, *Phys. Rev. B* **61**, R11879 (2000).
- [26] T. Hotta, A. Feiguin, and E. Dagotto, Stripes Induced by Orbital Ordering in Layered Manganites, *Phys. Rev. Lett.* **86**, 4922 (2001).
- [27] H. Aliaga, D. Magnoux, A. Moreo, D. Poilblanc, S. Yunoki, and E. Dagotto, Theoretical study of half-doped models for manganites: Fragility of CE phase with disorder, two types of colossal magnetoresistance, and charge-ordered states for electron-doped materials, *Phys. Rev. B* **68**, 104405 (2003).
- [28] S. Dong, Q. Zhang, S. Yunoki, J.-M. Liu, and E. Dagotto, Magnetic and orbital order in $(\text{RMnO}_3)_n/(\text{AMnO}_3)_{2n}$ superlattices studied via a double-exchange model with strain, *Phys. Rev. B* **86**, 205121 (2012).
- [29] P. G. Radaelli, D. E. Cox, M. Marezio, and S.-W. Cheong, Charge, orbital, and magnetic ordering in $\text{La}_{0.5}\text{Ca}_{0.5}\text{MnO}_3$, *Phys. Rev. B* **55**, 3015 (1997).
- [30] R. Hull and J. C. Bean, Misfit dislocations in lattice-mismatched epitaxial films, *Crit. Rev. Solid State Mater. Sci.* **17**, 507 (1992).
- [31] J. M. Rondinelli and N. A. Spaldin, Structure and Properties of Functional Oxide Thin Films: Insights From Electronic-Structure Calculations, *Adv. Mater.* **23**, 3363 (2011).
- [32] Y. Ogimoto, M. Nakamura, N. Takubo, H. Tamaru, M. Izumi, and K. Miyano, Strain-induced crossover of the metal-insulator transition in perovskite manganites, *Phys. Rev. B* **71**, 060403 (2005).
- [33] J. Roqueta, A. Pomar, L. Balcells, C. Frontera, S. Valencia, R. Abrudan, B. Bozzo, Z. Konstantinović, J. Santiso, and B. Martínez, Strain-Engineered Ferromagnetism in LaMnO_3 Thin Films, *Cryst. Growth Des.* **15**, 5332 (2015).
- [34] X. R. Wang, C. J. Li, W. M. Lü, T. R. Paudel, D. P. Leusink, M. Hoek, N. Poccia, A. Vailionis, T. Venkatesan, J. M. D. Coey, E. Y. Tsymbal, null, and H. Hilgenkamp, Imaging and control of ferromagnetism in $\text{LaMnO}_3/\text{SrTiO}_3$ heterostructures, *Science* **349**, 716 (2015).
- [35] H. Banerjee and M. Aichhorn, Emergence of a ferromagnetic insulating state in $\text{LaMnO}_3/\text{SrTiO}_3$ heterostructures: Role of strong electronic correlations and strain, *Phys. Rev. B* **101**, 241112 (2020).
- [36] Z. Zhang, J. Shao, F. Jin, K. Dai, J. Li, D. Lan, E. Hua, Y. Han, L. Wei, F. Cheng, B. Ge, L. Wang, Y. Zhao, and W. Wu, Uniaxial Strain and Hydrostatic Pressure Engineering of the Hidden Magnetism in $\text{La}_{1-x}\text{Ca}_x\text{MnO}_3$ ($0 \leq x \leq 1/2$) Thin Films, *Nano Lett.* **22**, 7328 (2022).
- [37] J. Guo, B. He, Y. Han, H. Liu, J. Han, X. Ma, J. Wang, W. Gao, and W. Lü, Resurrected and Tunable Conductivity and Ferromagnetism in the Secondary Growth $\text{La}_{0.7}\text{Ca}_{0.3}\text{MnO}_3$ on Transferred SrTiO_3 Membranes, *Nano Lett.* **24**, 1114 (2024).
- [38] S. Li, Z. Lu, B. Lao, X. Zheng, G. Chen, R.-W. Li, and Z. Wang, Cooperatively tuning magnetic anisotropy and colossal magnetoresistance via atomic-scale buffer layers in highly strained $\text{La}_{0.7}\text{Sr}_{0.3}\text{MnO}_3$ films, *Appl. Phys. Lett.* **124**, 172403 (2024).
- [39] C. Adamo, X. Ke, H. Q. Wang, H. L. Xin, T. Heeg, M. E. Hawley, W. Zander, J. Schubert, P. Schiffer, D. A. Muller, L. Maritato, and D. G. Schlom, Effect of biaxial strain on the electrical and magnetic properties of (001) $\text{La}_{0.7}\text{Sr}_{0.3}\text{MnO}_3$ thin films, *Appl. Phys. Lett.* **95**, 112504 (2009).
- [40] A. Vailionis, H. Boschker, W. Siemons, E. P. Houwman, D. H. A. Blank, G. Rijnders, and G. Koster, Misfit strain accommodation in epitaxial ABO_3 perovskites: Lattice rotations and lattice modulations, *Phys. Rev. B* **83**, 064101 (2011).
- [41] Y. Zhang, J. Liu, Y. Dong, S. Wu, J. Zhang, J. Wang, J. Lu, A. Rückriegel, H. Wang, R. Duine, H. Yu, Z. Luo, K. Shen, and J. Zhang, Strain-Driven Dzyaloshinskii-Moriya Interaction for Room-Temperature Magnetic Skyrmions, *Phys. Rev. Lett.* **127**, 117204 (2021).
- [42] Y. Takamura, R. V. Chopdekar, E. Arenholz, and Y. Suzuki, Control of the magnetic and magnetotransport properties of $\text{La}_{0.67}\text{Sr}_{0.33}\text{MnO}_3$ thin films through epitaxial strain, *Appl. Phys. Lett.* **92**, 162504 (2008).
- [43] Y. Wu, Y. Suzuki, U. Rüdiger, J. Yu, A. D. Kent, T. K.

- Nath, and C. B. Eom, Magnetotransport and magnetic domain structure in compressively strained colossal magnetoresistance films, *Appl. Phys. Lett.* **75**, 2295 (1999).
- [44] D. Lu, D. J. Baek, S. S. Hong, L. F. Kourkoutis, Y. Hikita, and H. Y. Hwang, Synthesis of freestanding single-crystal perovskite films and heterostructures by etching of sacrificial water-soluble layers, *Nat. Mater.* **15**, 1255 (2016).
- [45] J. Zhang, T. Lin, A. Wang, X. Wang, Q. He, H. Ye, J. Lu, Q. Wang, Z. Liang, F. Jin, S. Chen, M. Fan, E.-J. Guo, Q. Zhang, L. Gu, Z. Luo, L. Si, W. Wu, and L. Wang, Super-tetragonal $\text{Sr}_4\text{Al}_2\text{O}_7$ as a sacrificial layer for high-integrity freestanding oxide membranes, *Science* **383**, 388 (2024).
- [46] S. S. Hong, M. Gu, M. Verma, V. Harbola, B. Y. Wang, D. Lu, A. Vailionis, Y. Hikita, R. Pentcheva, J. M. Rondinelli, and H. Y. Hwang, Extreme tensile strain states in $\text{La}_{0.7}\text{Ca}_{0.3}\text{MnO}_3$ membranes, *Science* **368**, 71 (2020).
- [47] G. Kresse and J. Furthmüller, Efficient iterative schemes for ab initio total-energy calculations using a plane-wave basis set, *Phys. Rev. B* **54**, 11169 (1996).
- [48] J. P. Perdew, A. Ruzsinszky, G. I. Csonka, O. A. Vydrov, G. E. Scuseria, L. A. Constantin, X. Zhou, and K. Burke, Restoring the Density-Gradient Expansion for Exchange in Solids and Surfaces, *Phys. Rev. Lett.* **100**, 136406 (2008).
- [49] H. Park, A. J. Millis, and C. A. Marianetti, Density functional versus spin-density functional and the choice of correlated subspace in multivariable effective action theories of electronic structure, *Phys. Rev. B* **92**, 035146 (2015).
- [50] H. Park, A. J. Millis, and C. A. Marianetti, Site-Selective Mott Transition in Rare-Earth-Element Nickelates, *Phys. Rev. Lett.* **109**, 156402 (2012).
- [51] B. Lau and A. J. Millis, Theory of the Magnetic and Metal-Insulator Transitions in $R\text{NiO}_3$ Bulk and Layered Structures, *Phys. Rev. Lett.* **110**, 126404 (2013).
- [52] S. Johnston, A. Mukherjee, I. Elfimov, M. Berciu, and G. A. Sawatzky, Charge Disproportionation without Charge Transfer in the Rare-Earth-Element Nickelates as a Possible Mechanism for the Metal-Insulator Transition, *Phys. Rev. Lett.* **112**, 106404 (2014).
- [53] M. T. Fernández-Díaz, J. A. Alonso, M. J. Martínez-Lope, M. T. Casais, J. L. García-Muñoz, and M. A. G. Aranda, Charge disproportionation in $R\text{NiO}_3$ perovskites, *Physica B* **276–278**, 218 (2000).
- [54] M. Medarde, C. Dallera, M. Grioni, B. Delley, F. Vernay, J. Mesot, M. Sikora, J. A. Alonso, and M. J. Martínez-Lope, Charge disproportionation in $R\text{NiO}_3$ perovskites ($R = \text{rare earth}$) from high-resolution x-ray absorption spectroscopy, *Phys. Rev. B* **80**, 245105 (2009).
- [55] M. Ziese, H. C. Semmelhack, and K. H. Han, Strain-induced orbital ordering in thin $\text{La}_{0.7}\text{Ca}_{0.3}\text{MnO}_3$ films on SrTiO_3 , *Phys. Rev. B* **68**, 134444 (2003).
- [56] P. K. Siwach, H. K. Singh, and O. N. Srivastava, Influence of strain relaxation on magnetotransport properties of epitaxial $\text{La}_{0.7}\text{Ca}_{0.3}\text{MnO}_3$ films, *J. Phys.: Condens. Matter* **18**, 9783 (2006).
- [57] X. Ye, J. Zhao, H. Das, D. Sheptyakov, J. Yang, Y. Sakai, H. Hojo, Z. Liu, L. Zhou, L. Cao, T. Nishikubo, S. Wakazaki, C. Dong, X. Wang, Z. Hu, H.-J. Lin, C.-T. Chen, C. Sahle, A. Efiminko, H. Cao, S. Calder, K. Mibu, M. Kenzelmann, L. H. Tjeng, R. Yu, M. Azuma, C. Jin, and Y. Long, Observation of novel charge ordering and spin reorientation in perovskite oxide PbFeO_3 , *Nat. Commun.* **12**, 1917 (2021).
- [58] A. Prodi, A. Daoud-Aladine, F. Gozzo, B. Schmitt, O. Lebedev, G. van Tendeloo, E. Gilioli, F. Bolzoni, H. Aruga-Katori, H. Takagi, M. Marezio, and A. Gauzzi, Commensurate structural modulation in the charge- and orbitally ordered phase of the quadruple perovskite $(\text{NaMn}_3)\text{Mn}_4\text{O}_{12}$, *Phys. Rev. B* **90**, 180101 (2014).
- [59] K. Yang, D. I. Khomskii, and H. Wu, Unusual layered order and charge disproportionation in the double-perovskite compound $\text{Ca}_2\text{FeMnO}_6$, *Phys. Rev. B* **98**, 085105 (2018).
- [60] C. Şen and E. Dagotto, Properties of $\text{La}_{0.7}\text{Ca}_{0.3}\text{MnO}_3$ under extreme tensile strain, *Phys. Rev. B* **102**, 035126 (2020).
- [61] P. Rivero, V. Meunier, and W. Shelton, Uniaxial pressure-induced half-metallic ferromagnetic phase transition in LaMnO_3 , *Phys. Rev. B* **93**, 094409 (2016).
- [62] J. H. Lee, K. T. Delaney, E. Bousquet, N. A. Spaldin, and K. M. Rabe, Strong coupling of Jahn-Teller distortion to oxygen-octahedron rotation and functional properties in epitaxially strained orthorhombic LaMnO_3 , *Phys. Rev. B* **88**, 174426 (2013).
- [63] B. H. Kim and B. I. Min, Nearest and next-nearest superexchange interactions in orthorhombic perovskite manganites $R\text{MnO}_3$ ($R = \text{rare earth}$), *Phys. Rev. B* **80**, 064416 (2009).
- [64] M. W. Kim, S. J. Moon, J. H. Jung, J. Yu, S. Parashar, P. Murugavel, J. H. Lee, and T. W. Noh, Effect of Orbital Rotation and Mixing on the Optical Properties of Orthorhombic $R\text{MnO}_3$ ($R = \text{La, Pr, Nd, Gd, and Tb}$), *Phys. Rev. Lett.* **96**, 247205 (2006).
- [65] G. Zheng and C. H. Patterson, Ferromagnetic polarons in $\text{La}_{0.5}\text{Ca}_{0.5}\text{MnO}_3$ and $\text{La}_{0.33}\text{Ca}_{0.67}\text{MnO}_3$, *Phys. Rev. B* **67**, 220404 (2003).
- [66] B. H. Kim and B. I. Min, Effect of orbital symmetry on the anisotropic superexchange interaction, *New J. Phys.* **13**, 073034 (2011).
- [67] S. W. Jang, S. Ryee, H. Yoon, and M. J. Han, Charge density functional plus U theory of LaMnO_3 : Phase diagram, electronic structure, and magnetic interaction, *Phys. Rev. B* **98**, 125126 (2018).
- [68] M. B. Salamon and M. Jaime, The physics of manganites: Structure and transport, *Rev. Mod. Phys.* **73**, 583 (2001).

**Supplementary Information for “Direction-selective intertwined
charge, orbital, and lattice orders under uniaxial strain in
hole-doped manganite: $\text{La}_{0.75}\text{Ca}_{0.25}\text{MnO}_3$ ”**

Ju Hyeon Lee,¹ Beom Hyun Kim,^{2,*} and Bongjae Kim^{1,†}

¹*Department of Physics, Kyungpook National University, Daegu 45166, Republic of Korea*

²*Department of Physics & Astronomy,
Seoul National University, Seoul 08826, Republic of Korea*

Contents

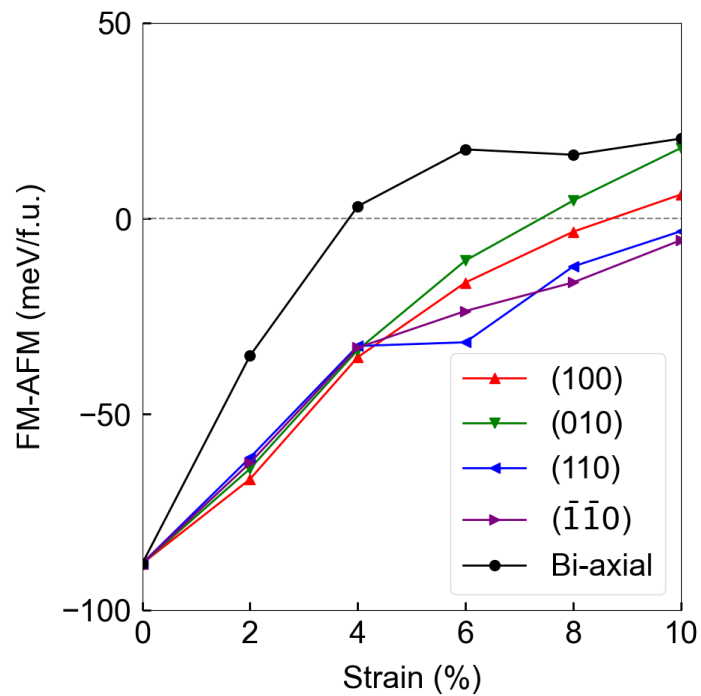
Crystal structure	2
Relative energy for ground state magnetic order	3
Lattice parameter	4
Bond length	5
Distortion and angle for LaMnO_3	6
Magnetic moment for strained $\text{La}_{0.75}\text{Ca}_{0.25}\text{MnO}_3$	7
Supplementary References	7

Crystal structure

Supplementary Table S1. Comparison of the experimental and calculated structures for different Hubbard parameters. The calculations were performed using the PBEsol functional with a tetragonal $\sqrt{2} \times \sqrt{2} \times 1$ unit cell containing one formula unit. In the main text, we used $U = 4$ eV and $J_H = 1$ eV [S1, S2].

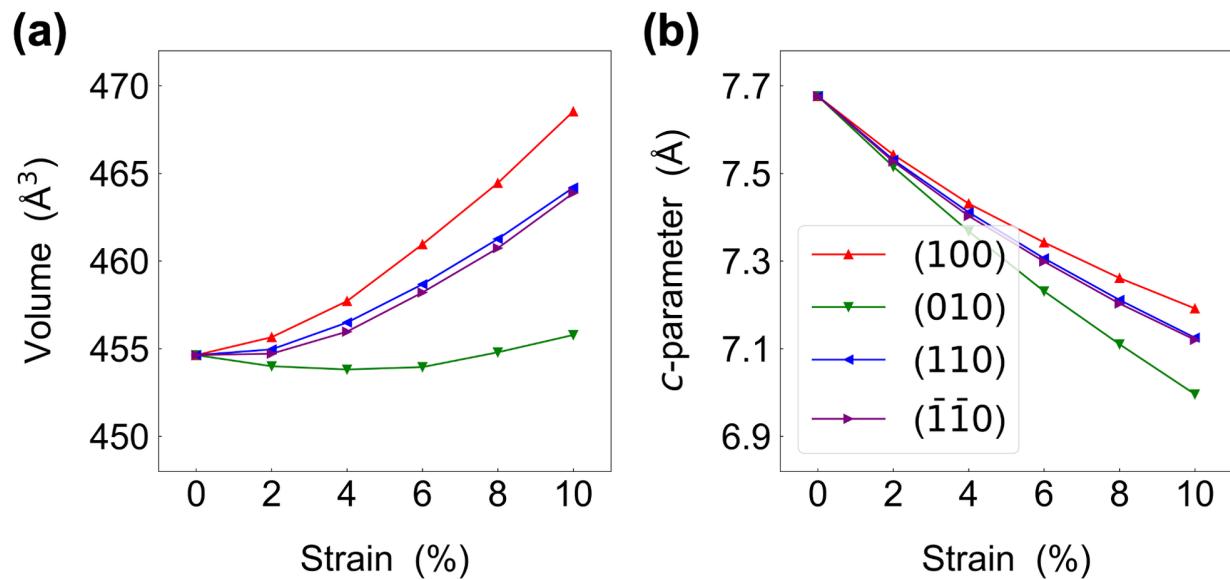
Type	$a = b$ (Å)	c (Å)	volume (Å ³)
Exp	5.459	7.701	229.49
PBEsol	5.416	7.639	224.05
PBEsol ($U = 4.0$ eV, $J_H = 1.0$ eV)	5.442	7.676	227.32
PBEsol ($U = 4.0$ eV, $J_H = 0.7$ eV)	5.436	7.668	226.60
PBEsol ($U = 6.0$ eV, $J_H = 1.0$ eV)	5.455	7.695	228.95

Relative energy for ground state magnetic order



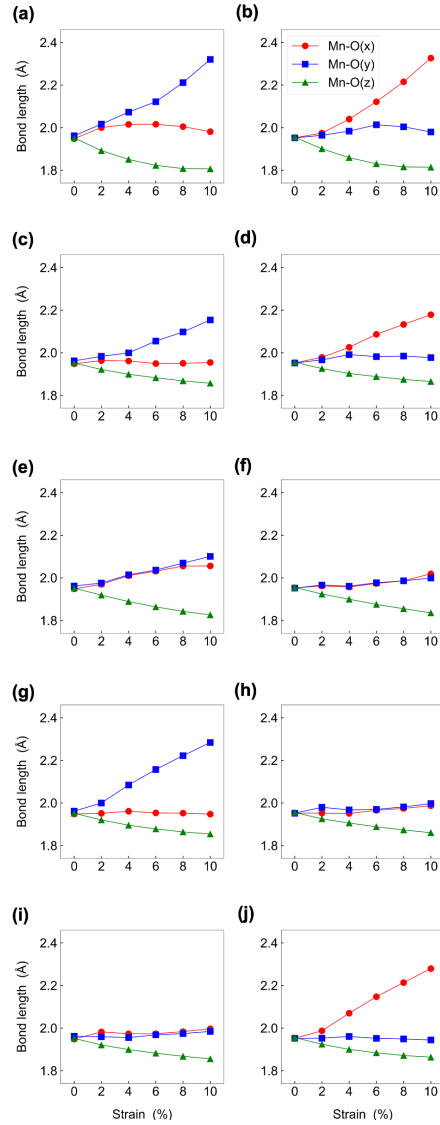
Supplementary Figure S1. Relative energy difference between the FM and *A*-type AFM states. The black, red, green, blue, and purple curves denote biaxial strain and uniaxial strain applied along the (100), (010), (110), and ($\bar{1}\bar{1}0$) directions, respectively.

Lattice parameter



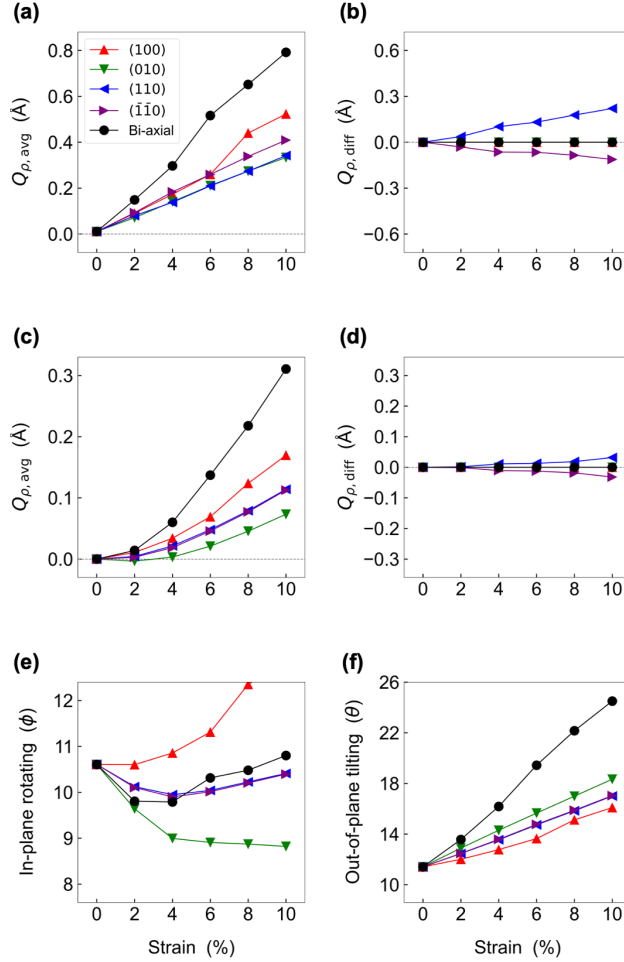
Supplementary Figure S2. Strain dependence of the volume and lattice parameter c , shown in (a) and (b), respectively. The red, green, blue, and purple curves correspond to uniaxial strain along the (100), (010), (110), and $(\bar{1}\bar{1}0)$ directions, respectively.

Bond length



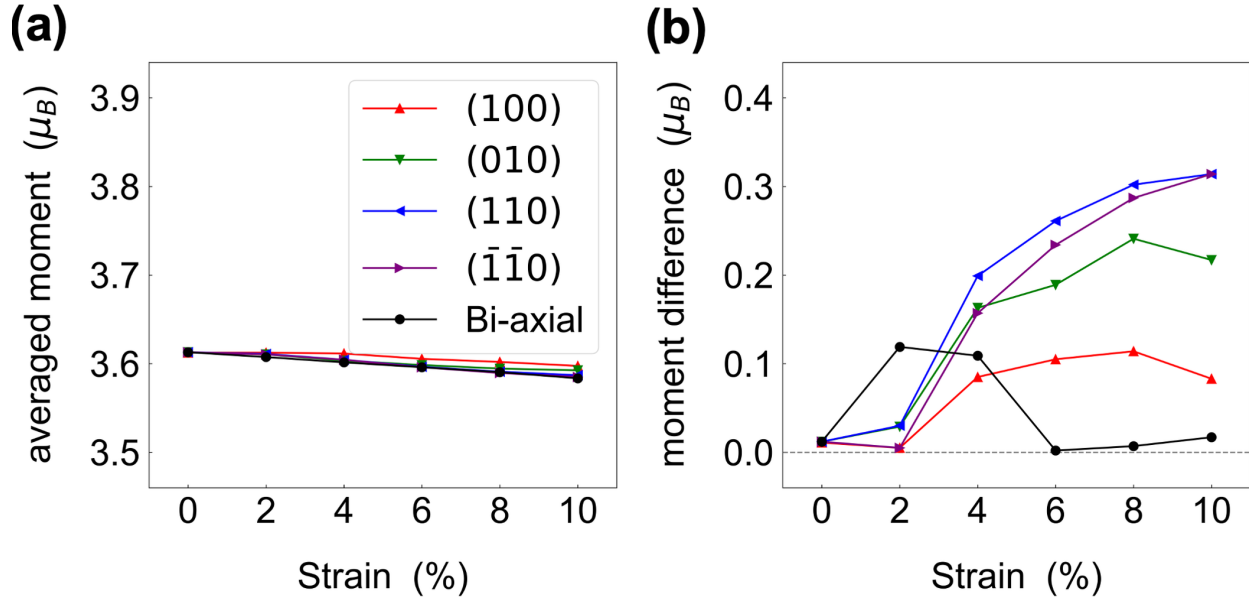
Supplementary Figure S3. Mn–O bond lengths as functions of strain. Panels (a), (c), (e), (g), and (i) correspond to octahedral site 1, while panels (b), (d), (f), (h), and (j) correspond to site 2. Panels (a) and (b) show the biaxial-strain case; (c) and (d), strain along (100); (e) and (f), strain along (010); (g) and (h), strain along (110); and (i) and (j), strain along $(\bar{1}\bar{1}0)$. The red, blue, and green curves denote the Mn–O bond lengths X , Y , and Z respectively, along the local axes x , y , and z (Fig. 2 (a)).

Distortion and angle for LaMnO₃



Supplementary Figure S4. Jahn-Teller distortion strengths are shown in (a) and (b), corresponding to the average and site-difference components, respectively. Panels (c) and (d) show the Q_1 distortion for the two octahedral sites, while (e) and (f) show the Mn–O–Mn angles associated with the in-plane rotation (ϕ) and out-of-plane tilt (θ), respectively. The corresponding angles and octahedral sites are illustrated in Fig. 2 (a). The corresponding angles and octahedral-site labels are illustrated in Fig. 2(a). For the undoped case, the Ca atoms in the LCMO cell were switched with La, and the structure was fully relaxed under the same constraints on the a and b lattice parameters as described in the main text. The black, red, green, blue, and purple curves denote biaxial strain and uniaxial strain applied along the (100), (010), (110), and ($\bar{1}\bar{1}0$) directions, respectively.

Magnetic moment for strained $\text{La}_{0.75}\text{Ca}_{0.25}\text{MnO}_3$



Supplementary Figure S5. The average magnetic moments and their site differences are shown in (a) and (b), respectively. The black, red, green, blue, and purple curves denote biaxial strain and uniaxial strain applied along the (100), (010), (110), and $(\bar{1}\bar{1}0)$ directions, respectively.

Supplementary References

* bomisu@gmail.com

† bongjae@knu.ac.kr

- [S1] S. S. Hong, M. Gu, M. Verma, V. Harbola, B. Y. Wang, D. Lu, A. Vailionis, Y. Hikita, R. Pentcheva, J. M. Rondinelli, and H. Y. Hwang, Extreme tensile strain states in $\text{La}_{0.7}\text{Ca}_{0.3}\text{MnO}_3$ membranes, *Science* **368**, 71 (2020).
- [S2] J. H. Lee and B. Kim, Revisiting LaMnO_3 : A density functional theory study, *Curr. Appl. Phys.* **78**, 7 (2025).